Energy Storage Materials 75 (2025) 104042

Contents lists available at ScienceDirect

Energy Storage Materials

journal homepage: www.elsevier.com/locate/ensm

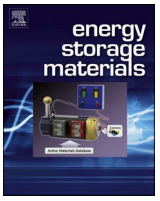

Structural response of silicon-containing graphite anodes on lithium intercalation

T. Hölderle [a,b,#], D. Petz [a,b,#], V. Kochetov [b], V. Baran [b,c], A. Kriele [d], Z. Hegedüs [c], U. Lienert [c], M. Avdeev [e,f], P. Müller-Buschbaum [a], A. Senyshyn [a,b,*]

[a] Department of Physics, Chair for Functional Materials, TUM School of Natural Sciences, Technical University of Munich, James-Franck Straße 1, 85748 Garching, Germany
[b] Heinz Maier-Leibnitz Zentrum (MLZ), Technical University of Munich, Lichtenbergstraße 1, 85748 Garching, Germany
[c] Deutsches Elektronen Synchrotron (DESY), Notkestraße 85, 22607 Hamburg, Germany
[d] German Engineering Materials Science Centre (GEMS) at Heinz Maier-Leibnitz Zentrum (MLZ), Helmholtz-Zentrum Hereon, Lichtenbergstraße 1, 85748 Garching, Germany
[e] Australian Centre for Neutron Scattering, Australian Nuclear Science and Technology Organisation (ANSTO), New Illawarra Rd, Lucas Heights NSW 2234, Sydney, Australia
[f] School of Chemistry, University of Sydney, NSW 2006, Sydney, Australia

A B S T R A C T

This study investigates the impact of silicon content in the graphite anode of cylinder-type Li-ion batteries using *operando* neutron powder diffraction techniques. A batch of four different Li-ion cells is analyzed, with a focus on the structural response of active cell components during electrochemical cycling. The results indicate that high silicon content in the graphite anode causes a delay in the initial lithiation of graphite, shifting it towards higher voltages independent of the cell's internal resistance. Differential voltage, incremental capacity analyses and quantitative energy-dispersive X-ray spectroscopy, corroborate these structural changes. Additionally, X-ray diffraction computed tomography using a μm-sized synchrotron beam revealed local structural degradation and lithiation inhomogeneity in the high silicon content cells during cycling.

1. Introduction

In recent years, the demand for high-performance energy storage systems has experienced a continuous rise due to the increasing need for portable electronic devices, electric vehicles, and the integration of renewable energy in society [1–3]. Thus, Lithium-ion batteries (LIBs) have emerged as the leading candidate for such applications due to their high energy/power densities and good cycling stability [4]. The graphite-based anode has been the common negative electrode material in LIBs since their commercialization. It is used in most state-of-the-art batteries nowadays due to its high theoretical specific capacity of approximately 372 mAh/g and high structural stability during the electrochemical de-/intercalation of Li ions in its structure [2,5,6]. However, to meet the requirements of the growing progress and to achieve even higher energy densities with an improved electrochemical battery performance at low costs, one has to switch from the pure graphite electrode design to exploring alternative electrode materials. Nowadays, one of the most encouraging materials for LIBs are silicon-based electrodes, which have emerged as a potential solution due to a low working voltage, high abundance, low cost and to the significantly higher lithiation capacity of silicon compared to graphite in the range of 4200 mAh/g, when fully lithiated to $Li_{4.4}Si$ [7,8]. However, the practical usage of silicon anodes yields significant challenges, where the substantial volume change experienced by silicon during de-/lithiation processes is pre-dominant. As lithium ions are inserted into silicon, its structure undergoes a considerable expansion of approximately 300 %, leading to high mechanical stress within the electrode [9–11]. The repeated volume changes during cycling result in silicon particle fracturing, pulverization, and loss of electrical contact, leading to capacity fading and a decreased cycle life as well as the destabilization of the solid electrolyte interface (SEI) [7]. Such problems can be alleviated and overcome (at least in part) by the design of nano-crystalline silicon powders and composites [12–14], usage of silicon nanowires [15,16], the utilization of protective coatings or with enhanced SEI stability and most promisingly, by merging graphite and silicon to a composite material, exhibiting relatively high energy densities, increasing structural

* Corresponding author.
E-mail address: anatoliy.senyshyn@gmail.com (A. Senyshyn).
# Authors contributed equally.

https://doi.org/10.1016/j.ensm.2025.104042
Received 29 October 2024; Received in revised form 3 January 2025; Accepted 17 January 2025
Available online 19 January 2025

integrity and mitigating volume change-induced mechanical stress [17–22]. While in the past years the amount of silicon was in the range of 2–3 %w/w in the anode, increase of its content is needed making electric vehicles competitive with combustion engines [23]. Thus, novel cells were developed using higher amounts of silicon in their anode and showing combined higher gravimetric and volumetric energy densities. Therefore, understanding of the interplay between the storage of lithium ions in graphite and silicon during the electrochemical cycling and its corresponding mechanical and structural impact on the electrochemical performance of the silicon-graphite composite is of vital importance. Materials, such as silicon, experience a transition from a crystalline to amorphous state upon electrochemical alloying (Li_xSi), [24,25]. While the electrochemically driven lithiation of silicon is accompanied by the loss of long-range order, due to its amorphization, the detection of its structural signatures, similar to those applied to graphite anodes, with diffraction techniques is non-trivial [23,26,27]. However, X-Ray diffraction techniques can be of use to study the Li redistribution in Si-graphite anodes indirectly [28], for example by neutron diffraction, which is a highly sensitive and advanced probe for non-destructive characterisation of the lithiation graphite anodes (either silicon-containing or not) due to its sensitivity to light elements like lithium [29]. These techniques, when used in combination, enable a multimodal approach to map the state of the cell non-destructively and with high precision on various length- and time-scales [30–32].

In the current study, different commercial LIBs are investigated to analyze the impact of silicon-containing graphite anodes on the diffraction signature of cycled LIBs, carrying out systematic neutron powder diffraction techniques. The samples are measured *operando* at low currents to map the de-/lithiation of silicon-containing graphite anodes in detail. The focus is set on the delayed intercalation of lithium ions into the graphite structure. In addition, the effect of aging on anodes with high silicon content, is further investigated with diffraction and imaging techniques, focusing on the degradation of the cell electrodes and the role of silicon in this process.

2. Experimental

2.1. Galvanostatic Cycling

Four different types of lithium-ion cells, LG INR21700 50H (short: 50H), Samsung INR21700 40T (short: 40T), Panasonic NCR18650 B [33,34] (Short: NNP), and LG INR18650 HG2 (short: HG2) with different manufacturer's specifications were analyzed. Cell types, selected specifications, and cycling parameters are listed in Table 1. Furthermore, incremental capacity analysis (ICA) and differential voltage analysis (DVA) calculations during charging with corresponding diffraction data are presented in the SI (Fig. S1-S4) as well.

2.2. Neutron powder diffraction

High-resolution neutron powder measurements were performed *operando* at the powder diffractometer ECHIDNA at the Australian Nuclear Science and Technology Organization (ANSTO, Sydney) [35] for cells 50H, 40T and HG2. The instrument was used in Debye-Scherrer configuration with a vertically focusing Ge (*331*) monochromator and a high monochromator take-off angle of 140°, supplying a monochromatic neutron beam with a wavelength of $\lambda = 2.44$ Å and a tailored size of 20 × 45 mm^2 at the sample position. The detection of scattered neutrons was carried out by a curved multidetector consisting of 128 position sensitive ^{3}He tubes, covering a 158.75° angular range [35]. The data acquisition was carried out with 20 steps and a detector step size of 0.125° with an exposure time per diffraction pattern of approx. 15 min. The samples were connected *via* soldered cables to a Biologic SP-300 Potentiostat and were mounted at the beamline on the gripper of the EPSON robotic sample changer [36]. Data collection was performed upon continuous cell rotational oscillation carried out by the robotic arm in the range of [−180:180°].

Additionally, *operando* high-resolution neutron powder measurements were carried out at SPODI [37–39] (FRM II, MLZ, Germany) on the NNP cell (data taken from Ref. [40] and previously reported in Refs. [41,42]) with experimental parameters similar to these mentioned above. The used wavelength of $\lambda = 2.536$ Å is maintained by the vertical focusing germanium monochromator (*331*) at 155° take-off angle with a beam size of 20 × 40 mm^2. The cell was mounted at the sample goniometer and connected to a Biologic VMP3 Potentiostat for electrochemical cycling. The vertical sensitive curved multidetector at SPODI consists of 80 ^{3}He detector tubes and Soller collimators (10′) in front. Stepwise positioning of the detector was achieved with 40 steps and 0.05° 2θ offset/resolution step to cover the angular range of 160°. Diffraction data were acquired with 45 s exposure per step resulting in a total acquisition time of ca. 30 min per pattern.

2.3. X-ray Diffraction computed tomography (XRD-CT)

In addition to *operando* diffraction measurements, XRD-CT was used to probe non-destructively and locally the structure and the lithium distribution of the electrodes within a fresh and an aged 50 H cell at a state-of-charge (SOC) of 100 %. The studies were carried out at the Swedish materials science beamline P21.2 [43] at PETRA III synchrotron (DESY, Hamburg) in Debye-Scherrer geometry with a monochromatic photon beam of $\lambda = 0.1503$ Å (fixed photon energy of 82.45 keV), focused to a beam size of 3 × 8 μm^2. Data was collected with a DECTRIS EIGER 2X CdTe 4M detector with a sample-to-detector distance of 1.382 m. The samples were mounted and pre-aligned at a goniometer head placed on the large goniometer of the main diffractometer. The diffraction tomography dataset was collected by horizontally scanning over a range of 22 mm with 550 translation steps at 825 individual angles ranging over 360° cell rotation. The data set was collected for one horizontal plane in the center of the cell. Data reduction and radial integration were done using the python library PyFAI [44,45]. The XRD-CT dataset was reconstructed with the filtered back-projection algorithm as implemented in the MATLAB suite.

2.4. X-ray Computed tomography (X-ray CT)

The configuration and structural deformation of the 50H cell after the electrochemical cycling was non-destructively mapped in a fully charged state using X-ray CT at a phoenix v|tome|x 240 s CT system (GE) equipped with a DXR-250RT CCD detector coupled to a CsI scintillator (200 × 200 mm^2 field of view, with 200 × 200 μm^2 pixel size and ~ 27 μm pixel resolution). Data was collected with an acceleration voltage set to 120 kV and a current of 100 μA using a direct tube at a focus-to-

Table 1
Specifications of the studied cells.

Manufacturer	Name	Cell type	Q [mAh]	Voltage [V]	Cathode	Silicon content [%w/w]	Cycling CCCV [mA]	Rest phase [h]	R_{int} [mΩ]
LG	INR21700 50H	21700	5000	2.0 – 4.2	NMC	10.5	200	5	33.2
LG	INR18650 HG2	18650	3000	2.0 – 4.2	NMC	4.6	250	1	52.4
Samsung	INR21700 40T	21700	4000	2.5 – 4.2	NCA	4.7	300	1	28.4
Panasonic	NCR18650 B	18650	3350	2.5 – 4.2	NCA	0	75	1	228.8

detector distance of 800.358 mm, collecting over the angular range of 360° with 1001 projections. The reconstruction of the data was carried out using the software X-AID and rendering of the reconstructed data was done using the open-source software package Paraview [46], and ImageJ [47].

2.5. Scanning electron microscopy (SEM)

Morphology and elemental composition of the electrodes of the aged 50H cell were analyzed *post mortem* using a ThermoFisher Scientific Quattro S field emission environmental scanning electron microscope (ESEM), which is operated jointly by the Helmholtz-Zentrum Hereon and the Jülich Center for Neutron Science (JCNS). The qualitative and quantitative studies were conducted using a standard Evenhart-Thornley secondary electron detector (ETD), sensitive to the material's topography, and a circular backscattered electron detector (CBS), sensitive to material contrast at 15 kV and 880 pA probe current. In addition, energy-dispersive X-ray spectroscopy was carried out with a ThermoFisher EDS UltraDry-Si-drift detector for mapping elemental composition. For cross-section measurements, an Ion Milling System ArBlade 5000 by Hitachi was used to prepare wide cross-sections of 2 mm within the extracted electrodes. Argon milling was carried out with an acceleration voltage set to 7.5 kV and a current of 600 μA. The airtight transport of the electrodes between the glovebox and the SEM or milling system was maintained by an airtight sample holder delivered by Hitachi and the one reported in Ref. [48].

3. Results and discussion

The obtained *operando* diffraction datasets consist of diffraction contributions from the positive electrode ($LiNiMnCoO_2$ (NMC), or $LiNiCoAlO_2$ (NCA)), the negative electrode made up of graphite/silicon composite, the separator, either aluminum (cathode) or copper (anode) current collectors, the steel housing, and center pin. The organic electrolyte and the dissolved lithium salt ($LiPF_6$) are in a liquid (short-range ordered) state, scattering incoherently and contributing to the background in the collected data. During the electrochemical cycling, various structural changes can be detected, either by a series of phase transitions dedicated to the lithiation of the graphite [49] or by a shift of the positive electrode reflections due to its lithium de/-intercalation, visible for each cell analyzed (Fig. S1). However, the focus is set on the influence and structural response of the amount of silicon contained in the negative electrode of the cells. In Fig. 1, the interatomic spacing *d* of the *003* cathode reflection, as well as the first order *00l*($l = 1, 2$) reflections of the intercalated graphite, are plotted against the normalized capacity during the charging process for the cells 50H, 40T, NNP, and HG2. All cells display a similar behavior for the *003* reflection of the $NaCrS_2$-type cathode. While there is a constant shift of the *d* spacing towards higher capacities, the slope displays gradual changes starting at ca. 80 % SOC, showing a maximum *interatomic* spacing at 4.85 Å before returning back to a lower *d* spacing of 4.65 Å at high SOCs. The observed behavior is already well known and can be attributed to the deintercalation of lithium ions from the cathode host structure, causing a structural change visible by an increase in the unit cell dimension *c* followed by a subsequent decrease [40]. The negative electrode also responds to the potential change *via* an intercalation mechanism of 2H graphite already reported in Ref. [48,49]. Intercalation starts from a pure graphite phase with interatomic distances of 3.35 Å, followed by a continuous transition[1] - the coexistence of low lithiated phases (Li_xC_6 with $x < 0.5$) - and a biphasic intercalation behavior represented by stage II - LiC_{12} (3.5 Å) and stage I - LiC_6 (3.7 Å) (Fig. S2). Note: a similar behavior occurs for the second-order reflections of 00*l*type (Fig. S3).

On the contrary, due to its short-range structural order and relatively low chemical content, no dedicated diffraction signal from silicon was observed in the diffraction measurements using thermal neutrons. The onset of observed phase transitions, whose signatures are visible in the diffraction data, can directly be associated with the calculated peaks of the DVA plotted in Fig. 1, while the peaks in the ICA (Fig. S2) indicate the phase transitions itself. DVA calculations show dedicated peaks following a similar profile for all cells, and are consistent with the data reported by Ref. [50]. At low SOC, indicated by the blue area (Fig. 1), the DVA data of cells 50H, 40T, and HG2 display a characteristic shoulder, which is missing in the DVA data of the NNP cell, followed by a DVA valley. At higher SOC (gray area), three distinct peaks are observed, representing the lithiation stages of graphite 4L, 3L, and 2L [51]. The following peak (G_2) corresponds to stage 2 of lithiated graphite, and indicates the onset of the phase transition from LiC_{12} to LiC_6 phase, which marks 50 % of the graphite lithiation [52]. The final peak observed in the DVA data corresponds to the onset of the phase transition of the cathode, marking decreasing *d* spacings of the *003* reflection. Complementary, the calculated ICA peaks were observed in accordance with the characteristic valleys of the DVA data, describing a plateau in the classical capacity/voltage plot (Fig. S4a-d).

Observed characteristic signals at both DVA and ICA data can be associated with the phase change of the electrode materials. Besides this, further differences in the DVA signals can be distinguished by the SOC at which the signals occur. Thus, the first DVA peak in the 50H cell arises at higher SOC (~30 %), when compared to the 40T/HG2 cell (~22 %), and the NNP cell (~13 %). In addition, a similar behavior is observed in the ICA data, showing the lowest voltage ICA peak in the 50H cell arising at a higher potential (3.5 V), in contrast to the 40T/HG2 cell (3.45 V) and the NNP cell (3.36 V), thus creating a specific "voltage delay" taking place at the initial stage of Li intercalation in the graphite. Furthermore, the observed delay correlates with the appearance of a shoulder visible at the lowest voltage ICA peak, strongly pronounced in the 50H data, more minor in the 40T/HG2 data, and not present in the NNP data (Fig. 1).

Experimentally observed systematic behavior raises questions about the cause and origin of such structural and electrochemical peculiarities. Analysis of the internal apparent resistance (Table 1) of the cells, calculated at the initial voltage drop during discharge according to $R_{DC} = (V_0 - V_t)/(I_0 - I_t)$ [54], yields values that cannot solely explain the observed SOC shifts. For example, the 50H and 40T cells (displaying the first intercalation of graphite at the highest potentials during charging) possess internal resistances at the lowest edge compared to the other cells. Both 50H and 40T cells are of 21700-type, while the remaining studied cells are of 18650-type, inhibiting a higher internal resistance [55] naturally. Instead, a shift of the initial lithiation of graphite towards higher SOC is attributed directly to an increasing silicon content in the graphite electrode [26], indicating an additional lithiation occurring before the graphite lithiation. In other words, silicon-containing graphite displays a multistep lithiation behavior, where a lithiation of the silicon grains occurs first with a subsequent lithiation of the remaining graphite structure. The lithiation of silicon prior to graphite arises from their different standard potentials (Potential, V vs. Li^+/Li), where silicon has a standard potential of 0.4 V and graphite has a standard potential of 0.1 V [56,57]. The higher standard potential of silicon compared to graphite results in an increased thermodynamic preference (driving force) for lithium-ions alloying with the silicon (reduction) rather than intercalating into the graphite. After the full lithiation of silicon is finished, lithium ions can additionally intercalate into the graphite structure [58], as it becomes apparent from diffraction data. The shift of DVA peaks towards higher SOC in all the cells can be unambiguously correlated with the amount of silicon contained in the electrode, which corresponds to the alloying of lithium with silicon. In line with this, the NNP cell represents a graphite electrode with small or no amount of silicon, the 40T and HG2 cell possesses

[1] Limited experimental resolution does not permit detailed observation of diffraction signal from lithium intercalated graphite stage 3L and 4L reported in the literature [49].

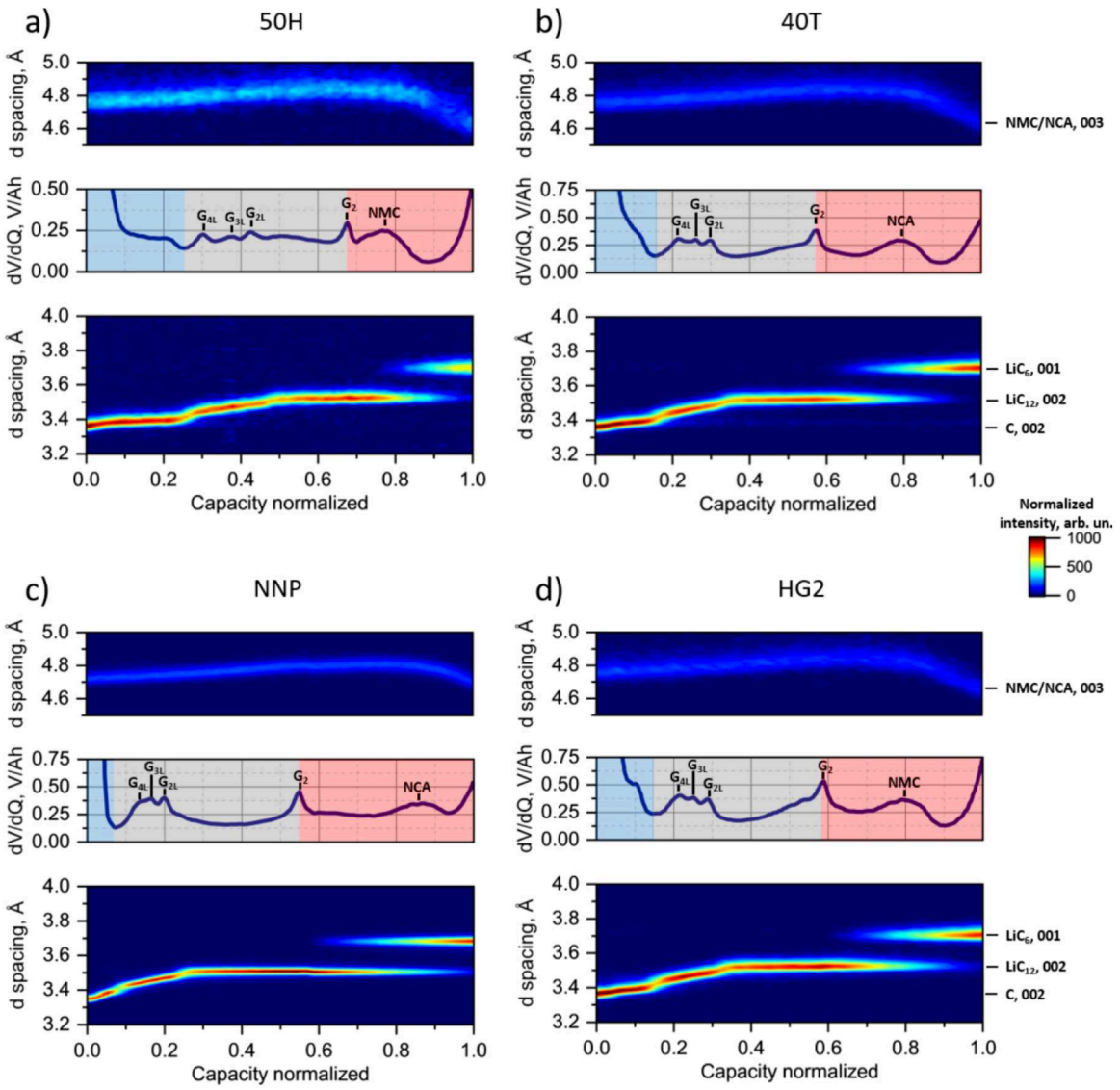

Fig. 1. Differential voltage analysis (DVA) combined with powder diffraction data for different commercial lithium-ion cells (a) 50H, (b) 40T, (c) NNP [40], and (d) HG2, showing structural response of normalized reflection intensities, and electrochemical response, with corresponding DVA peaks marking onsets of dedicated graphite stages (4L, 3L, 2L, 2) and cathode (NMC/NCA) phase transitions [50,51]. The background color marks silicon lithiation (blue) [53], the lithiation in solid solution regime Li_xC_6 with $x \leq 0.5$ (gray), and the final lithiation of graphite to LiC_6 (red).

a certain (non-zero) silicon content, and the 50H shows the highest silicon content of all cells with more than 20 % capacity attributed to the lithiation of silicon.

To validate this assumption, EDX measurements were carried out to reveal the amount of silicon in the anode (Table S1) and cathode (Table S2), quantitatively. The measurements revealed no silicon within the NNP negative electrode, while the highest amount of silicon (10.5 % w/w) is observed for the 50H cell (Table 1). The remaining cells contain a moderate (intermediate) silicon content (4.6 – 4.7 %w/w). This suggests that an increasing content of silicon is directly associated with the growing delay in the graphite lithiation, having experimental signatures

(i) by the shift of DVA peaks, representing graphite stages, towards higher SOC;
(ii) by the shift of the initial graphite lithiation towards higher voltages, visible in the diffraction data;
(iii) by the increasing shoulder size close to the lowest voltage peak in the ICA data.

While the increasing amount of silicon in the negative electrode has a positive effect on the cell capacity, increasing energy density, it negatively influences the structural integrity of the cells due to the substantial volume expansion. To characterize this effect, the 50H cell was aged by continuous cycling. The electrochemical cycling (detailed parameters in SI) was carried out until the state-of-health (SOH) of the cell fell below 80 %. The cycling showed a linear capacity decrease > 82 % SOH with a subsequent acceleration of capacity degradation at this level, potentially marking a different degradation regime during the cell aging (Fig. S5a). The ICA signal during aging (Fig. S6) displays a decrease in its intensity, due to capacity loss and a shift towards higher/lower voltages during charging/discharging for almost all peaks, due to increasing internal cell resistance, unambiguously reflecting the cell degradation. Reference electrochemical measurements performed at SOH < 80 % revealed a decrease in the intensity and a shift of the first ICA peak 1a (with a decrease and a shift of its shoulder, accordingly) towards higher voltages, which may be attributed to silicon degradation in the battery anode. The effect co-exists with a *quasi* linear increase of internal resistance (as confirmed by R_{DC} estimations) mediating the potential window and cell self-heating (Fig. S5b) [59].

Besides electrochemical characterizations, a set of studies focusing

on the structural degradation of the cell and its electrodes was performed. The internal layout of the fully charged 50H cell was probed non-destructively using X-ray CT measurements at distinct states, namely fresh one, after 100-, and 400-cycles, and at the end of cycling. It has been found that the cell is built on a classical high-energy cell scheme with negative current tabs near the cell housing (35 mm in height), and close to the center pin (57 mm in height) located on the anode electrode strip (Fig. S7). The positive current tab (64 mm in height) is located within the cathode electrode strip by ca. 48 cm away from the beginning of the cathode strip, starting at the center of the cell. The overall length of the anode is slightly longer with respect to the cathode, where the negative electrode extends beyond the edge of the positive strip at its beginning and end, with ca. 3 ½ windings in surplus. The electrodes are wound up as a stack of alternating layers of double-coated cathode electrode strips (on Al current collector), separator, and double-sided coated anode electrode (on Cu current collector), yielding a ~240 µm (fresh state), and ~250 µm thick electrode stack after ~700 cycles (Fig. S8), respectively. This is confirmed by individual SEM cross-section measurements (Fig. 2c) corresponding to 115 µm thick double-sided cathode strip, consisting of a 25 µm thick Al current collector with two 45 µm thick coated cathode layers; the double-sided anode strip displays a total thickness of 115 µm, consisting of two 50 µm thick anode layers coated double-sided on a 15 µm thick Cu current collector.

The effect of extended electrochemical cycling is directly visible in the X-ray CT data, showing a deformation of the electrode spiral in the 50H cell. In the fresh state, the cell shows a relatively ordered structure of the winded electrodes, forming a regular spiral. However, close to the center of the cell, the beginning of the cathode strip is sandwiched between the anode ones, causing the anode layers to fold locally. During electrochemical cycling, the structural expansion and contraction of electrodes [60] results in the rearrangement of the electrode strips. Such movement leads to deformation, cracking, and exfoliation and proceeds to the fold of the electrode layers/windings with increasing cycle number (Fig. 2b) [61,62].

Besides the morphological changes, rapid cell aging typically results in the non-homogeneous lithium/electrolyte distribution at various length scales [63,64]. XRD-CT was applied to probe the interior of the 50H cell non-destructively at 50 % cell height. With 40 µm effective resolution, one can resolve structural information of double-coated electrode layers, the separator, and the cell housing with their individual signals in the mean diffraction patterns (see Fig. S9). For the anode, the lithiation was estimated from fractional molar concentrations, calculated from diffraction intensities associated with different lithiated graphite phases (see SI). Corresponding reconstructed anode lithiation across the cell displays a uniform distribution for the fresh cell, with regions of low lithiation corresponding to the current tabs positions and the overlap of the anode at the endpoints of the anode strip [65]. Intensities of the *110* Fe, and *200* Al peaks (which cannot be distinguished due to the overlap of the diffraction signals) correspond to the cell housing and the current collector of the cathode strip (Fig. S10). In the fresh state the anode displays a high and uniform lithiation over the whole electrode thickness (Fig. 2a). Due to the loss of lithium inventory, aging causes the overall lithiation of the anode to decrease, which is accompanied by the increase of heterogeneity, i.e., the inhomogeneous lithiation over the electrodes' thickness and length. In addition, the deformation of the electrode layers also influenced the lithiation of the anode, due to the bending of the current collector, as visible in the reconstructed Al+Fe reflections (Fig. S10). Thus, the lithiation is lower along the tear-off, and higher at the neighboring fold. Similar to the fresh cell, locations of lowest lithiation in the aged cell were observed at the current tabs position and the endpoints of the electrode strips (Fig. S10). In addition, a lithiation gradient was observed over the cross-section of the aged cell. While such behavior is hard to follow in the reconstructed image, the lithiation x in Li_xC_6 was decomposed into an average value $\langle x \rangle$ and its deviation Δx as $x = \langle x \rangle \pm \Delta x$ with Δx plotted at Fig. 3a (fresh - top and aged - bottom).

The calculated average value decreased from an initial 0.96 in a fresh state to ~70 % of the initial value (0.65) in an aged state, while the observed capacity showed a loss of ~20 % after cycling (700 cycles) in the electrochemical data. This discrepancy arises due to the additional capacity contributed by the silicon, which is not taken into account for the calculated average lithium content in the graphite. Within the calculated deviations, lithium non-uniformities can be observed from

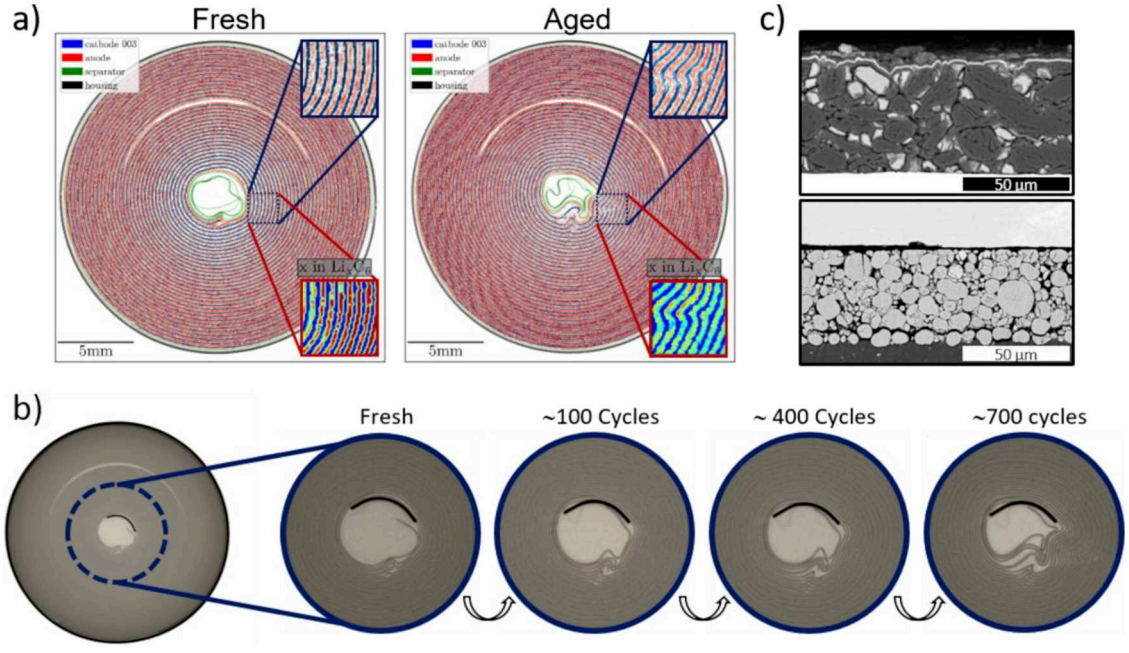

Fig. 2. Interior (electrode layout) of 50H cell. XRD-CT measurements (a) of the fresh and aged 50H cells, showing internal structural degradation, lithiation of region of interest and intensities of anode, cathode, separator, and housing (mean patterns and selected phases in Fig. S9/10); X-ray CT measurements (b) of 50H cell at different SOH showing the structural deformation of electrode layers during electrochemical cycling; cross-section SEM images (c) of the extracted aged anode (upper image) and cathode (lower image) coated on current collectors.

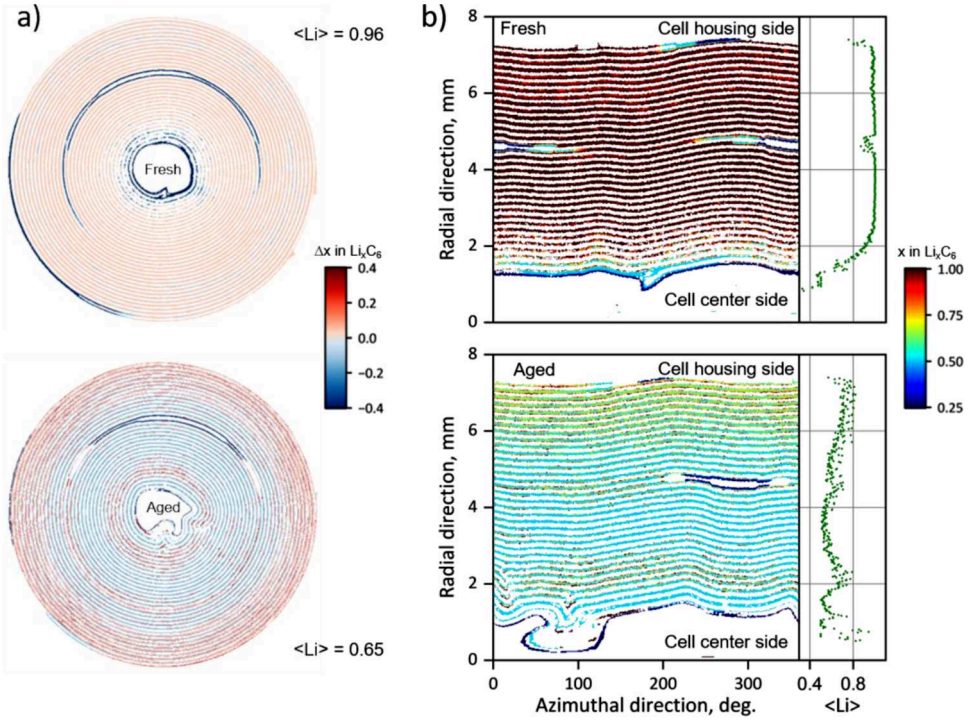

Fig. 3. Deviation from lithium distribution (a) and virtual electrode unrolling (b) for the 50H cell in a fresh and in an aged state.

the aged cell's outer region towards the inner of the aged cell, showing a higher lithiation starting from the cell housing followed by a region of decreasing lithiation at half the cell's radius. Towards the center of the cell, the lithiation increased with a subsequent decrease, marked by the ending of the cathode strip. In addition, the reconstructed images were virtually unrolled by transformation into polar coordinates (Fig. 3b: fresh - top, and aged – bottom) to bypass the circular geometry of the 50H cell [31], and to focus on the electrode stack thickness (Fig. S11), calculated from unrolled reconstructed Fe and Al intensities (detailed description in SI). While the electrodes of the fresh stack show a smaller average thickness of 248 ± 14 µm, electrochemical aging of the cell results in an increased average electrode stack thickness of 254 ± 17 µm.[2] Furthermore, the thickness of the electrodes varies across the cell diameter. The highest thickness was observed at the endpoints of the electrodes, and locally at the position of the positive current tab, within the jelly roll, as observed by Ref. [66]. Thus, the degradation of the electrodes results in an average increase in layer thickness. In contrast, the thickness variations along the length of the electrodes are degradation-independent, as observed in the fresh and aged state.

To add more detail, a set of SEM measurements was carried out *post-mortem* on the aged 50H cell (Fig. S12). Surface morphology measurements revealed a homogeneous distribution of graphite and silicon particles; while the graphite grains display a more regular (round) shape, the silicon grains/flakes show a more edgy shape, forming together a relatively rough surface (Fig. S13). Contrary to the anode, the cathode surface is more structured, with particle sizes smaller than those of graphite. However, some grains display a fractured morphology, while others display irregularities (Fig. S14). When zooming into the cathode cross-section (Fig. S12), similar morphological features persist: most of the cathode grains are fractured, creating a strong contrast to the negative electrode displaying layer-like structure with overall less deformation than the cathode grains. Probing the silicon grain composition with EDX revealed signals from silicon, oxygen, and magnesium (Fig. S15). This may point to the small addition of magnesium to enhance cycling stability upon maintaining structural integrity [67]. However, such structures decrease the effective capacity of the silicon and do not contribute to Li storage during the electrochemical cycle [67–70]. A small dark layer on the surface of silicon grains can be localized as well and the corresponding EDX signal is composed from fluorine, phosphorous, and sulfur. While the fluorine and phosphorous could be attributed to residues of the electrolyte and lithium salt ($LiPF_6$) [48], the detected sulfur is likely to be a part of the silicon coating [71–74].[3]

4. Conclusion

The structural and electrochemical behavior of commercial LIBs with varying silicon content in the graphite-based negative electrode was examined. *Operando* neutron diffraction techniques are utilized to monitor structural changes during electrochemical cycling, with a particular emphasis on the influence of silicon content on the negative electrode. The sequential lithiation of silicon and graphite during charging, driven by their different standard potentials, is observed, with silicon undergoing lithiation at lower cell potentials compared to graphite. This sequential lithiation causes an increasingly delayed structural response in the graphite as the silicon content in the electrode increases. Independent DVA and ICA analyses corroborate the diffraction data, demonstrating that cells with higher silicon content exhibit distinct electrochemical characteristics, including phase transitions at increased SOCs/voltages, as evidenced by the shift of DVA/ICA peaks, and the appearance of a characteristic shoulder in the data for 50H cell (containing the highest silicon content), in contrast to the NNP cell (with no silicon), as confirmed by EDX measurements. The 50H cell, due to its

[2] The small averaged deviations affecting the estimates from X-Ray CT are expected, due to the unrolling process and averaging with deformed electrodes.

[3] A positive effect of silicon nanoparticle coating with sulfur on cycling rate and performance of silicon anodes is reported [71,72], as well as Nafion [73], a proton conductor membrane used as SEI on silicon oxide grains [74], containing a sulfonate group, and suiting to the detected fluorine and sulfur signals of the EDX measurements.

high silicon content, exhibits the highest energy density, prompting further investigation of its morphological and structural evolution, particularly the effects of silicon volume expansion during cycling. The aging process was tracked until the 50H cell's SOH reaches < 80 %, revealing an initial linear capacity degradation followed by accelerated aging, coinciding with the decrease of the characteristic shoulder in the ICA data, which is attributed to the degradation of silicon.

Multiscale analysis using X-ray CT, XRD-CT, and SEM revealed significant inhomogeneities in graphite lithiation, electrode deformation, particle cracking, particularly in the cathode grains, and electrode delamination, all of which adversely impacted cell lithiation and performance. Besides this, aging-induced swelling and non-uniform thickness variations within the electrode stack are also observed, directly affecting the mechanical integrity of the cell. EDX analysis identified the presence of magnesium silicon oxide particles, with fluorine and sulfur coatings on the silicon grains.

In conclusion, while silicon within the graphite electrode is in an amorphous state, its presence can be unambiguously inferred from the delayed lithiation of graphite. Increased silicon content enhances the energy density of Li-ion cells, which, however, is supplemented by the remarkable structural degradation, leading to a loss of silicon lithiation and/or non-uniform anode lithiation, which detrimentally affects cell lifespan and performance. Future research should prioritize improving the structural stability and integrity of silicon-containing electrodes either alone or in combination with cathodes to reconcile the advantages of increased energy density with the need for long-term durability and stability.

CRediT authorship contribution statement

T. Hölderle: Writing – review & editing, Writing – original draft, Visualization, Methodology, Investigation, Formal analysis, Conceptualization. **D. Petz:** Writing – review & editing, Visualization, Validation, Software, Methodology, Investigation, Formal analysis, Conceptualization. **V. Kochetov:** Writing – review & editing, Visualization, Validation, Software, Methodology, Formal analysis. **V. Baran:** Writing – review & editing, Resources, Investigation, Data curation. **A. Kriele:** Writing – review & editing, Investigation, Formal analysis, Data curation. **Z. Hegedüs:** Writing – review & editing, Resources, Data curation. **U. Lienert:** Writing – review & editing, Resources, Data curation. **M. Avdeev:** Writing – review & editing, Resources, Data curation. **P. Müller-Buschbaum:** Writing – review & editing, Supervision, Resources, Project administration, Funding acquisition. **A. Senyshyn:** Writing – review & editing, Writing – original draft, Supervision, Resources, Project administration, Methodology, Funding acquisition, Conceptualization.

Declaration of competing interest

The authors declare that they have no known competing financial interests or personal relationships that could have appeared to influence the work reported in this paper.

Acknowledgments

The authors gratefully acknowledge the financial support provided by the Heinz Maier-Leibnitz Zentrum (Technische Universität München), German Federal Ministry of Education and Research (BMBF project 05K19VK3) and German Research Foundation (DFG, project MU 1487/36-1). Authors wish to thank the Australian Center for Neutron Scattering of the Australian Nuclear Science and Technology Organisation (ANSTO) for the provision of beamtime allocated for proposal(s) P13478 the Heinz Maier-Leibnitz Zentrum for the provision of beamtime and access to their infrastructure; DESY (Hamburg, Germany), a member of the Helmholtz Association HGF, for the provision of experimental facilities (Petra III) P02.1 and P21.2. Beamtime was allocated for proposal(s) I-20190614, I-20231235.

Supplementary materials

Supplementary material associated with this article can be found, in the online version, at doi:10.1016/j.ensm.2025.104042.

References

[1] M. Armand, J.M. Tarascon, Building better batteries, Nature 451 (7179) (2008) 652–657.
[2] B. Scrosati, J. Garche, Lithium batteries: status, prospects and future, J. Power Sources 195 (9) (2010) 2419–2430.
[3] B. Dunn, H. Kamath, J.-M. Tarascon, Electrical energy storage for the grid: a battery of choices, Science (1979) 334 (6058) (2011) 928–935.
[4] J.B. Goodenough, K.-S. Park, The Li-Ion rechargeable battery: a perspective, J. Am. Chem. Soc. 135 (4) (2013) 1167–1176.
[5] M. Winter, et al., Insertion electrode materials for rechargeable lithium batteries, Adv. Mater. 10 (10) (1998) 725–763.
[6] A. Senyshyn, et al., Lithium Intercalation into Graphitic Carbons Revisited: experimental Evidence for Twisted Bilayer Behavior, J. Electrochem. Soc. 160 (5) (2013) A3198.
[7] M.N. Obrovac, et al., Alloy design for lithium-ion battery anodes, J. Electrochem. Soc. 154 (9) (2007) A849.
[8] X. Zuo, et al., Silicon based lithium-ion battery anodes: a chronicle perspective review, Nano Energy 31 (2017) 113–143.
[9] S. Kalnaus, K. Rhodes, C. Daniel, A study of lithium ion intercalation induced fracture of silicon particles used as anode material in Li-ion battery, J. Power Sources 196 (19) (2011) 8116–8124.
[10] N. Nitta, et al., Li-ion battery materials: present and future, Mater. Today 18 (5) (2015) 252–264.
[11] R.A. Huggins, Materials science principles related to alloys of potential use in rechargeable lithium cells, J. Power Sources 26 (1) (1989) 109–120.
[12] M.N. Obrovac, L.J. Krause, Reversible cycling of crystalline silicon powder, J. Electrochem. Soc. 154 (2) (2007) A103.
[13] N. Liu, et al., A yolk-shell design for stabilized and scalable li-ion battery alloy anodes, Nano Lett. 12 (6) (2012) 3315–3321.
[14] A. Magasinski, et al., High-performance lithium-ion anodes using a hierarchical bottom-up approach, Nat. Mater. 9 (4) (2010) 353–358.
[15] L. Hu, et al., Si nanoparticle-decorated Si nanowire networks for Li-ion battery anodes, Chem. Commun. 47 (1) (2011) 367–369.
[16] L.-F. Cui, et al., Light-weight free-standing carbon nanotube-silicon films for anodes of lithium ion batteries, ACS Nano 4 (7) (2010) 3671–3678.
[17] I.H. Son, et al., Silicon carbide-free graphene growth on silicon for lithium-ion battery with high volumetric energy density, Nat. Commun. 6 (1) (2015) 7393.
[18] N. Liu, et al., A pomegranate-inspired nanoscale design for large-volume-change lithium battery anodes, Nat. Nanotechnol. 9 (3) (2014) 187–192.
[19] S. He, et al., Considering critical factors of silicon/graphite anode materials for practical high-energy lithium-ion battery applications, Energy & Fuels 35 (2) (2021) 944–964.
[20] X.H. Liu, et al., Size-dependent fracture of silicon nanoparticles during lithiation, ACS Nano 6 (2) (2012) 1522–1531.
[21] C. Xu, et al., Improved performance of the silicon anode for li-ion batteries: understanding the surface modification mechanism of fluoroethylene carbonate as an effective electrolyte additive, Chem. Mater. 27 (7) (2015) 2591–2599.
[22] J. Zhao, et al., Artificial solid electrolyte interphase-protected lixsi nanoparticles: an efficient and stable prelithiation reagent for lithium-ion batteries, J. Am. Chem. Soc. 137 (26) (2015) 8372–8375.
[23] J. Moon, et al., Interplay between electrochemical reactions and mechanical responses in silicon–graphite anodes and its impact on degradation, Nat. Commun. 12 (1) (2021) 2714.
[24] P. Limthongkul, et al., Electrochemically-driven solid-state amorphization in lithium-silicon alloys and implications for lithium storage, Acta Mater. 51 (4) (2003) 1103–1113.
[25] V.L. Chevrier, J.R. Dahn, First principles model of amorphous silicon lithiation, J. Electrochem. Soc. 156 (6) (2009) A454.
[26] H. Jung, et al., The structural and electrochemical study on the blended anode with graphite and silicon carbon nano composite in Li ion battery, Electrochim. Acta 245 (2017) 791–795.
[27] K.P.C. Yao, et al., Operando quantification of (de)lithiation behavior of silicon–graphite blended electrodes for lithium-ion batteries, Adv. Energy Mater. 9 (8) (2019) 1803380.
[28] C. Hogrefe, et al., Lithium redistribution mechanism within silicon-graphite electrodes: multi-method approach and method validation, J. Electrochem. Soc. 171 (7) (2024) 070503.
[29] O. Dolotko, et al., *Understanding structural changes in NMC Li-ion cells by* in situ *neutron diffraction*, J. Power Sources 255 (2014) 197–203.
[30] C.L. Berhaut, et al., Multiscale multiphase lithiation and delithiation mechanisms in a composite electrode unraveled by simultaneous operando small-angle and wide-angle x-ray scattering, ACS Nano 13 (10) (2019) 11538–11551.
[31] E. Lübke, et al., The origins of critical deformations in cylindrical silicon based Li-ion batteries, Energy Environ. Sci. 17 (14) (2024) 5048–5059.

[32] D. Atkins, et al., Accelerating Battery Characterization Using Neutron and Synchrotron Techniques: toward a Multi-Modal and Multi-Scale Standardized Experimental Workflow, Adv. Energy Mater. 12 (17) (2022) 2102694.
[33] M. Hagen, et al., Lithium–sulfur cells: the gap between the state-of-the-art and the requirements for high energy battery cells, Adv. Energy Mater. 5 (16) (2015) 1401986.
[34] W. Diao, C. Kulkarni, M. Pecht, Development of an informative lithium-ion battery datasheet, Energies (Basel) 14 (17) (2021) 5434.
[35] M. Avdeev, J.R. Hester, ECHIDNA: a decade of high-resolution neutron powder diffraction at OPAL, J. Appl. Crystallogr. 51 (6) (2018) 1597–1604.
[36] S. Olsen, S. Pullen, M. Avdeev, A 100-position robotic sample changer for powder diffraction with low-background vacuum chamber, J. Appl. Crystallogr. 43 (2) (2010) 377–379.
[37] M. Hoelzel, et al., High-resolution neutron powder diffractometer SPODI at research reactor FRM II, Nucle. Instrum. Methods Phys. Res. A: Accelerators, Spectrometers, Detectors and Associated Equipment 667 (2012) 32–37.
[38] M. Hoelzel, A. Senyshyn, O. Dolotko, SPODI: high resolution powder diffractometer, J. large-scale Res. Facil. JLSRF (2015) 1.
[39] R. Gilles, et al., First test measurements at the new structure powder diffractometer (SPODI) at the FRM-II, in: Ninth European Powder Diffraction Conference, Oldenbourg Wissenschaftsverlag, 2015.
[40] T. Hölderle, et al., The structural behavior of electrochemically delithiated, J. Power Sources 564 (2023) 232799.
[41] M.J. Mühlbauer, et al., Inhomogeneous distribution of lithium and electrolyte in aged Li-ion cylindrical cells, J. Power Sources 475 (2020) 228690.
[42] D. Petz, et al., Heterogeneity of Graphite Lithiation in State-of-the-Art Cylinder-Type Li-Ion Cells, Batter. Supercaps. 4 (2) (2021) 327–335.
[43] Z. Hegedüs, et al., Imaging modalities at the Swedish Materials Science beamline at PETRA III, IOP Conf. Ser. Mater. Sci. Eng. 580 (1) (2019) 012032.
[44] J. Kieffer, et al., New tools for calibrating diffraction setups, J. Synchrotron Radiat 27 (2) (2020) 558–566.
[45] G. Ashiotis, et al., The fast azimuthal integration Python library: pyFAI, J. Appl. Crystallogr 48 (2) (2015) 510–519.
[46] U. Ayachit, The ParaView Guide: A Parallel Visualization Application, Kitware, Inc, 2015.
[47] C.A. Schneider, W.S. Rasband, K.W. Eliceiri, NIH Image to ImageJ: 25 years of image analysis, Nat. Methods 9 (7) (2012) 671–675.
[48] T. Hölderle, et al., Thermal Structural Behavior of ElectrochemicallyLithiated Graphite (LixC6) Anodes in Li-ion Batteries, Batter. Supercaps. 7 (3) (2024) e202300499.
[49] C. Didier, et al., Phase evolution and intermittent disorder in electrochemically lithiated graphite determined using in operando neutron diffraction, Chem. Mater. 32 (6) (2020) 2518–2531.
[50] S. Ludwig, M. Steinhardt, A. Jossen, Determination of internal temperature differences for various cylindrical lithium-ion batteries using a pulse resistance approach, Batteries 8 (2022) 60.
[51] M. Ank, et al., Lithium-Ion Cells in Automotive Applications: tesla 4680 Cylindrical Cell Teardown and Characterization, J. Electrochem Soc. 170 (12) (2023) 120536.
[52] J.R. Dahn, Phase diagram of ${\mathrm{Li}}_{\mathit{x}}$${\mathrm{C}}_{6}$, Phys. Rev. B 44 (17) (1991) 9170–9177.
[53] J. Schmitt, M. Schindler, A. Jossen, Change in the half-cell open-circuit potential curves of silicon–graphite and nickel-rich lithium nickel manganese cobalt oxide during cycle aging, J. Power Sources 506 (2021) 230240.
[54] H.-G. Schweiger, et al., Comparison of Several Methods for Determining the Internal Resistance of Lithium Ion Cells, Sensors 10 (2010) 5604–5625.
[55] T. Waldmann, et al., *18650* vs. *21700 Li-ion cells – A direct comparison of electrochemical, thermal, and geometrical properties*, J. Power Sources 472 (2020) 228614.
[56] J. Li, et al., From materials to cell: state-of-the-art and prospective technologies for lithium-ion battery electrode processing, Chem. Rev. 122 (1) (2022) 903–956.
[57] M. Armand, et al., Lithium-ion batteries – Current state of the art and anticipated developments, J. Power Sources 479 (2020) 228708.
[58] C. Berg, et al., Comparison of silicon and graphite anodes: temperature-dependence of impedance characteristics and rate performance, J. Electrochem. Soc. 170 (3) (2023) 030534.
[59] L.B. Diaz, et al., Measuring irreversible heat generation in lithium-ion batteries: an experimental methodology, J. Electrochem. Soc. 169 (3) (2022) 030523.
[60] A. Pfrang, et al., Deformation from formation until end of life: micro x-ray computed tomography of silicon alloy containing 18650 Li-Ion Cells, J. Electrochem. Soc. 170 (3) (2023) 030548.
[61] R.F. Ziesche, et al., 4D imaging of lithium-batteries using correlative neutron and X-ray tomography with a virtual unrolling technique, Nat. Commun. 11 (1) (2020) 777.
[62] P. Blažek, et al., Multiscale 3D Analysis of Defects and Temporal Development of Electrode Morphology in Lithium-Ion Batteries By X-Ray Computed Tomography, ECS Trans. 105 (1) (2021) 69.
[63] D. Petz, et al., Lithium distribution and transfer in high-power 18650-type Li-ion cells at multiple length scales, Energy Storage Mater. 41 (2021) 546–553.
[64] D. Petz, et al., Aging-driven composition and distribution changes of electrolyte and graphite anode in 18650-type li-ion batteries, Adv. Energy Mater. 12 (45) (2022) 2201652.
[65] D. Petz, et al., Lithium heterogeneities in cylinder-type Li-ion batteries – fatigue induced by cycling, J. Power Sources 448 (2020) 227466.
[66] J. Jiang, et al., Mapping internal deformation in 4695 batteries through a combination of X-ray computer tomography and machine learning, J. Power Sources 621 (2024) 235130.
[67] B. Liu, et al., Mg-doped, carbon-coated, and prelithiated SiO as anode materials with improved initial Coulombic efficiency for lithium-ion batteries, Carbon Energy 6 (3) (2024) e421.
[68] J. Han, et al., Homogenizing Silicon Domains in SiOx Anode during Cycling and Enhancing Battery Performance via Magnesium Doping, ACS Appl.. Mater. Interfaces 13 (44) (2021) 52202–52214.
[69] B. Xu, et al., Improved cycling performance of SiOx/MgO/Mg2SiO4/C composite anode materials for lithium-ion battery, Appl. Surf. Sci. 546 (2021) 148814.
[70] W. Zhou, S. Upreti, M.S. Whittingham, High performance Si/MgO/graphite composite as the anode for lithium-ion batteries, Electrochem. Commun. 13 (10) (2011) 1102–1104.
[71] A. Baasner, et al., Sulfur: an intermediate template for advanced silicon anode architectures, J. Mater. Chem. A 6 (30) (2018) 14787–14796.
[72] W. Chen, et al., Stable and High-Rate silicon anode enabled by artificial Poly (acrylonitrile)–Sulfur interface engineering for advanced Lithium-ion batteries, J. Electroanal. Chem. 929 (2023) 117093.
[73] W.G. Grot, Nafion® membrane and its applications. Electrochemistry in Industry: New Directions, Springer, 1982, pp. 73–87.
[74] C. Shen, et al., Silicon(lithiated)–sulfur full cells with porous silicon anode shielded by Nafion against polysulfides to achieve high capacity and energy density, Nano Energy 19 (2016) 68–77.